AGU PUBLICATIONS

JGR

Journal of Geophysical Research: Solid Earth

RESEARCH ARTICLE
10.1002/2017JB014823

Key Points:
- We show a new approach for separating magnetic fabrics in carbonates, by combining AMS measurements at room and low temperatures and AARM
- Diamagnetic fabric of coccolith calcite indicates tectonic strain, and paramagnetic fabric of clays preserves the depositional fabric
- We suggest a mechanism of coccolith rotation, contributing to the development of AMS parallel to the maximum shortening direction

Correspondence to:
R. Issachar,
ranissachar@gmail.com

Citation:
Issachar, R., Levi, T., Marco, S., & Weinberger, R. (2018). Separation of diamagnetic and paramagnetic fabrics reveals strain directions in carbonate rocks. *Journal of Geophysical Research: Solid Earth*, *123*, 2035–2048. https://doi.org/10.1002/2017JB014823

Received 3 AUG 2017
Accepted 4 FEB 2018
Accepted article online 13 FEB 2018
Published online 10 MAR 2018

Separation of Diamagnetic and Paramagnetic Fabrics Reveals Strain Directions in Carbonate Rocks

R. Issachar[1,2], T. Levi[2], S. Marco[1], and R. Weinberger[2,3]

[1]Department of Geophysics, Tel Aviv University, Tel Aviv, Israel, [2]Geological Survey of Israel, Jerusalem, Israel, [3]Department of Geological and Environmental Sciences, Ben-Gurion University of the Negev, Beer-Sheva, Israel

Abstract We present a new procedure for separating magnetic fabrics in coccolith-bearing chalk samples, demonstrated in the case studies of three sites located within the Dead Sea Fault (DSF) plate boundary. The separation is achieved by combining measurements of room temperature and low-temperature anisotropy of magnetic susceptibility (RT-AMS and LT-AMS, respectively) with anisotropy of anhysteretic remanence magnetization (AARM). The LT-AMS, measured at ~77 K, enhances the fabric of paramagnetic clay minerals. The AARM represents the fabric of ferromagnetic Fe oxides. By subtracting the paramagnetic and ferromagnetic fabrics from the RT-AMS, the diamagnetic fabric is separated. In the studied samples, we found that the ferromagnetic contribution to the bulk magnetic fabric is negligible and could be excluded from the subtraction procedure. Our analysis indicates that in chalks with a negligible ferromagnetic contribution, diamagnetic fabric predominates the rock bulk magnetic fabric, if the mean susceptibility is $<-6\times10^{-6}$ SI, whereas with a mean susceptibility $>11\times10^{-6}$ SI, paramagnetic fabric predominates. In the studied rocks, the paramagnetic clay minerals preserve the original depositional fabric, whereas the diamagnetic minerals show a tectonic fabric. We propose a mechanism by which coccolith rotation under tectonic strain contributes to the development of the diamagnetic fabric parallel to the shortening direction. We infer that the diamagnetic fabrics of the studied rocks indicate strain regime of approximately N-S horizontal shortening near strands of the DSF system. This suggests a deflection of the regional principal strain axes near the DSF. The diamagnetic fabric is more sensitive to tectonic strain than paramagnetic fabric in chalks and provides a valuable strain indicator near major faults.

1. Introduction

Anisotropy of magnetic susceptibility (AMS) depicts the magnetic fabrics of rocks and is commonly used as a strain indicator (e.g., Borradaile, 1991; Borradaile & Henry, 1997; Braun et al., 2015; Cifelli et al., 2013; Levi, Weinberger, & Marco, 2014; Parés, van der Pluijm, & Dinares-Turell, 1999; Soto et al., 2007). AMS measurements at low field integrate diamagnetic, paramagnetic, and ferromagnetic fabrics and present the distribution of all minerals in a rock sample (Borradaile, 1988). The AMS of diamagnetic and paramagnetic minerals is controlled by crystallography, while the AMS of ferromagnetic minerals is also controlled by grain shape and distribution (Borradaile & Jackson, 2010). Different minerals in rocks may respond to strain in different manners and also may form at different times during the geological history (e.g., Borradaile et al., 2010; Levi, Weinberger, & Marco, 2014; Oliva-Urcia et al., 2016). Hence, it is useful to separate the mineral contributions (Martin-Hernandez & Ferre, 2007), particularly in rocks containing the competing effect of magnetic fabrics that may cancel each other (Hirt & Almqvist, 2011). Previous studies have demonstrated the need for separating the magnetic fabrics. For instance, Debacker et al. (2004) investigated the magnetic fabrics of cleaved pelitic rocks and suggested that different minerals were distributed between cleavage and bedding planes. Almqvist et al. (2011) found that in carbonate rocks, both diamagnetic and paramagnetic fabrics indicated tectonic deformations but differed in the correlation between the magnetic and strain axes. Levi, Weinberger, & Marco (2014) found that in soft sediments, the ferromagnetic fabric of titanomagnetite preserved the depositional fabric, while the diamagnetic fabric of aragonite was obliterated by faulting processes.

In this study, we focus on Eocene chalk formations, as they are widely exposed along the Dead Sea Fault (DSF) plate boundary and predate its early Miocene formation (Nuriel et al., 2017). The studied samples are from three sites located next to strands of the DSF (Figure 1). This study is a part of an ongoing effort to better

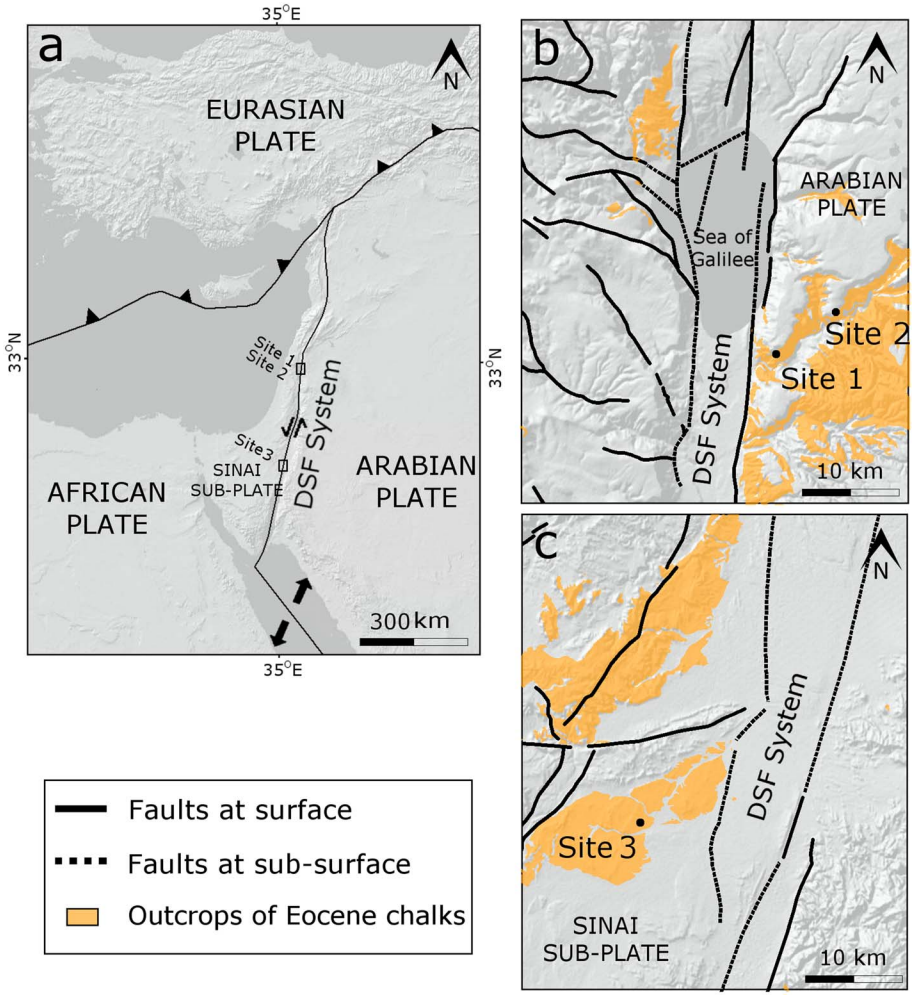

Figure 1. (a) General tectonic map showing the location of the study sites (boxes) along the Dead Sea Fault (DSF) system. (b and c) Geological maps of the studied sites after Sneh et al. (1998) and fault traces after Sneh and Weinberger (2014). Site 1 and Site 2 are located in the Arabian Plate, whereas Site 3 is located in the Sinai subplate.

understand the geological history of the DSF and its associated strain field. In recent studies, magnetic fabrics of pure calcite-bearing rocks revealed deflection of the principal strain axes next to strands of the DSF (Issachar et al., 2015; Levi & Weinberger, 2011). Although pure calcite-bearing rocks are considered excellent strain indicators (e.g., Issachar et al., 2015), they are rare and have limited distribution next to the DSF. The chalks investigated in this study consist of diamagnetic, paramagnetic, and ferromagnetic fabrics, and hence, the correlation of the bulk magnetic fabrics to the strain field is not straightforward. Improving the abilities to separate the magnetic fabrics in carbonate rocks allows a better estimation of the strain field near the DSF and in other tectonic settings where carbonates are exposed.

2. Separation of Magnetic Fabrics in Carbonate Rocks

The susceptibility of paramagnetic minerals increases with temperature decrease following the Curie-Weiss law, $k = C/(T - \theta)$, where C is the specific mineral Curie constant, T is the temperature in degrees Kelvin, and θ is the paramagnetic Curie temperature, which is zero for pure paramagnetic materials (e.g., Cullity, 1972). These physical characteristics help to separate the paramagnetic minerals from a carbonate matrix by measuring the AMS, both at room temperature (RT-AMS) and at low temperature (LT-AMS) (Martin-Hernandez & Ferre, 2007; Parés & van der Pluijm, 2002; Schmidt et al., 2007). The susceptibility of ferromagnetic minerals is usually much higher than the susceptibilities of diamagnetic and paramagnetic minerals

(Hunt et al., 1995; Rochette et al., 1992), suggesting that even minute amounts of ferromagnetic minerals in a rock sample significantly influence its AMS (e.g., Borradaile et al., 2010). The ferromagnetic minerals solely control the anisotropy of the magnetic remanence. Hence, it is possible to measure their magnetic fabrics directly, most commonly by anisotropy of anhysteretic remanence magnetization (AARM) technique (Bilardello & Jackson, 2014; Jackson, 1991). Nevertheless, the relationship between ferromagnetic AMS and AARM anisotropies is not straightforward and has to be carefully considered, depending on the mineralogy (Hrouda, 2002; Till et al., 2010). By measuring the RT-AMS, LT-AMS, and AARM of carbonate rock samples, the magnetic fabric of the diamagnetic, paramagnetic, and ferromagnetic fabrics can be analytically separated as described below.

The AMS is mathematically described as a second-rank symmetric tensor $\boldsymbol{k}$ with eigenvalues $k_1 \geq k_2 \geq k_3$ and eigenvectors $\boldsymbol{k_1}$, $\boldsymbol{k_2}$, and $\boldsymbol{k_3}$. The susceptibility tensor measured at room temperature ($\boldsymbol{k}^{RT}$) is described as the sum of all magnetic fabrics (Henry, 1983; Henry & Daly, 1983; Hrouda, Henry, & Borradaile, 2000):

$$\boldsymbol{k}^{RT} = c_d\boldsymbol{K}_d + c_p\boldsymbol{K}_p + c_f\boldsymbol{K}_f = \boldsymbol{k}_d + \boldsymbol{k}_p + \boldsymbol{k}_f, \tag{1}$$

where $\boldsymbol{K}_d$, $\boldsymbol{K}_p$, and $\boldsymbol{K}_f$ are the diamagnetic, paramagnetic, and ferromagnetic susceptibility tensors, respectively; c_d, c_p, and c_f are the respective percentages ($c_d + c_p + c_f = 1$); and $\boldsymbol{k}_d$, $\boldsymbol{k}_p$, and $\boldsymbol{k}_f$ are known as the respective susceptibility contribution tensors (Hrouda, Henry, & Borradaile, 2000).

The LT-AMS measured at low temperature amplifies the paramagnetic fabrics by a factor α, the paramagnetic amplification factor, which is the ratio between room temperature and low temperature. Hence, the susceptibility tensor measured at low temperature ($\boldsymbol{k}^{LT}$) is

$$\boldsymbol{k}^{LT} = c_d\boldsymbol{K}_d + \alpha \cdot c_p\boldsymbol{K}_p + c_f\boldsymbol{K}_f = \boldsymbol{k}_d + \alpha \cdot \boldsymbol{k}_p + \boldsymbol{k}_f \tag{2}$$

By subtracting equation (1) from equation (2), the paramagnetic susceptibility contribution tensor is analytically separated:

$$\boldsymbol{k}_p = \frac{\boldsymbol{k}^{LT} - \boldsymbol{k}^{RT}}{\alpha - 1} \tag{3}$$

This separation of $\boldsymbol{k}_p$ introduces experimental errors originating from both RT and LT measurements. In practice, the LT-AMS might represent the paramagnetic tensor more correctly than the analytical separation of equation (3). In this case, only the mean susceptibility of the paramagnetic fabrics (k_{mp}) is calculated from equation (3), as described below. A susceptibility tensor is often expressed as the product of mean susceptibility ($k_m = k_1 + k_2 + k_3/3$) and normalized tensor ($\widehat{\boldsymbol{k}}$). Consequently, $\boldsymbol{k} = k_m \cdot \widehat{\boldsymbol{k}}$ (Borradaile, Fralick, & Lagroix, 1999). The sample mean susceptibility is the sum of its diamagnetic, paramagnetic, and ferromagnetic mean susceptibilities, denoted k_{md}, k_{mp}, and k_{mf}, respectively. Hence, by subtracting LT and RT mean susceptibilities ($k_m{}^{LT}$and $k_m{}^{RT}$, respectively), the respective contribution mean susceptibility of the paramagnetic fabrics (k_{mp}) can be derived:

$$k_{mp} = \frac{k_m{}^{LT} - k_m{}^{RT}}{\alpha - 1}. \tag{4}$$

By measuring a number of samples from a site, a plot of $k_m{}^{LT}$ versus $k_m{}^{RT}$ could be presented. If k_{mp} varies between the samples, and k_{md} and k_{mf} are constant, a linear dependency is expected, as follows:

$$k_m{}^{LT} = \alpha \cdot k_m{}^{RT} + (1 - \alpha)(k_{md} + k_{mf}) \tag{5}$$

The slope of the linear regression is >1 and represents the paramagnetic amplification factor (α). The sum $k_{md} + k_{mf}$ is extracted from the intersection with $k_m{}^{LT}$axis. Likewise, the point where $k_m{}^{RT}$ and $k_m{}^{LT}$ are equal represents a k_m value that excludes the contribution of paramagnetic minerals (i.e., $k_{md} + k_{mf}$). In such a case, k_{mp} for each sample is

$$k_{mp} = k_m{}^{RT} - (k_{md} + k_{mf}), \tag{6}$$

where k_{mp} can be calculated for all the site samples without the need of measuring their LT-AMS. In carbonate rocks, the calcite content c_d (in percentages) can be derived from a chemical analysis, whereas its mean susceptibility value is well known from the literature (-12.87×10^{-6} SI) (Nye, 1957). Thus, a good estimate of k_{md} is practically available and, consequently, k_{mf} can be derived. In cases of a linear correlation

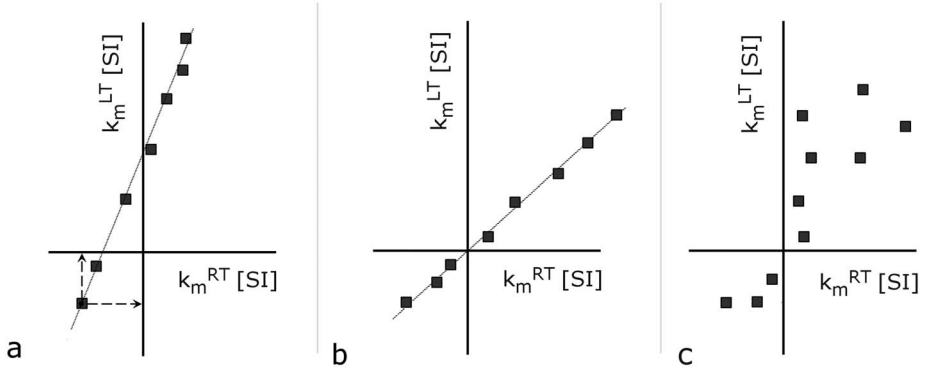

Figure 2. Schematic relationship between low-temperature and room temperature mean susceptibilities k_m^{LT} and k_m^{RT}, respectively. (a) Samples with constant diamagnetic and ferromagnetic contents and varied paramagnetic contents. The linear fit is good with a slope > 1. The point where $k_m^{LT} = k_m^{RT}$ (marked with arrows) indicates susceptibility value of $k_{md} + k_{mf}$. (b) Samples with no paramagnetic contribution. The linear fit is excellent with a slope of 1. (c) Samples with paramagnetic contribution and varied diamagnetic and/or ferromagnetic contents. The linear fit is poor.

between k_m^{LT} and k_m^{RT}, with $\alpha = 1$, the paramagnetic contribution is negligible; therefore, $k_{mp} = 0$ (Figure 2b). In cases where a linear correlation between k_m^{LT} and k_m^{RT} is poor (Figure 2c), the paramagnetic contribution is significant and k_{md} and/or k_{mf} vary between the samples. In such a case k_{mp} can be calculated only for samples that are measured by the RT-AMS and LT-AMS methods. AARM can provide a first-order approximation of the normalized ferromagnetic tensor $\widehat{\boldsymbol{k}}_f$, with the limitations described by Hrouda, Henry, & Borradaile (2000). By using the AARM method and equation (1), the diamagnetic normalized tensor is calculated:

$$k_{m_d} \cdot \widehat{\boldsymbol{k}}_d = k_m^{RT} \cdot \widehat{\boldsymbol{k}}^{RT} - k_{m_p} \cdot \widehat{\boldsymbol{k}}_p - k_{m_f} \cdot \widehat{\boldsymbol{k}}_{f'} \tag{7}$$

where $\widehat{\boldsymbol{k}}_d$ and $\widehat{\boldsymbol{k}}_p$ are the normalized diamagnetic and paramagnetic tensors, respectively. In summary, the ferromagnetic fabrics are separated by AARM measurements, the paramagnetic fabrics are separated by LT-AMS measurements, and the diamagnetic fabrics are separated by subtracting the paramagnetic and ferromagnetic fabrics from RT-AMS measurements.

3. Geological Setting

The DSF is a plate boundary between Arabia and Sinai subplate. It has been active since the early Miocene (Nuriel et al., 2017) and accommodates ~105 km of left-lateral offset (Freund et al., 1970; Quennell, 1959). A mesostructure analysis carried by Eyal and Reches (1983) and Eyal (1996) indicates regional NNW-SSE horizontal shortening (S_{Hmax}) associated with the left-lateral motion along the DSF system. The NNW-SSE strain field varies locally in the vicinity of the DSF, aligned either subparallel or subperpendicular to strands of the DSF system (Garfunkel, 1981; Weinberger, Gross, & Sneh, 2009).

We studied the magnetic fabrics of chalks in two areas located ~250 km apart along the DSF, the southern Golan Heights (Site 1 and Site 2) and Arava (Site 3) areas (Figure 1). Site 1 and Site 2 are located ~2 km and 8 km east of DSF strands on the Arabian Plate, respectively. The sampled subhorizontal chalk beds are part of the early Eocene Maresha Formation (Buchbinder & Gvirtzman, 1966). Site 3 is located in the central Arava valley in between the strands of the DSF system and about 15 km west of a major DSF strand. The sampled horizontal beds are part of the early Eocene Paran Formation (Benjamini, 1984). These chalk formations have high porosity (>20%) (Palchik & Hatzor, 2002) and may contain up to 25% clay fraction (Nathan & Flexer, 1977).

4. Methods

4.1. Petrography, Mineralogy, and Geochemistry

The petrography, mineralogy, and geochemistry of representative samples were studied in order to identify and characterize the mineral components and estimate their proportions in the rocks. The petrography of the

samples and their mineral assemblage were studied by extrahigh-resolution Scanning Electron Microscope (SEM) (Magellan TM 400L) at the Nano-characterization center at the Hebrew University of Jerusalem. The microscope is equipped with an EDS (Energy-dispersive X-ray spectroscopy) detector that enables spotted composition analyses.

Geochemical measurements were conducted in order to estimate the carbonate and clay portions in the rock and to measure Fe contents in the bulk rock and the carbonate fraction. A geochemical scheme was developed at the geochemical laboratories of the Geological Survey of Israel, allowing the determination of the chemical composition of different mineralogical components of the rock (see details in Braun et al., 2015). To estimate the chemical content of the bulk rock, 0.5 g was dissolved using $LiBO_4$, and the major element contents were measured using an Inductively Coupled Plasma Mass Spectrometer (Perkin Elmer OPTIMA 3300) (1 s $<$ 3% for Fe). To determine the chemical content of the carbonate fraction (calcite and dolomite), it was extracted from the rock using 50 mL of 1:5 HNO_3 for 0.4 g of bulk rock for 24 h. This procedure allows dissolving the carbonate without affecting the Al silicate and the Fe oxides fraction.

To evaluate the amount of clay and other Al-Si minerals in the rock, the insoluble residue procedure was used. One gram of bulk rock was dissolved in 1:1 concentrated HCl, and the insoluble residue was filtered and weighed. The %I.R. fraction was calculated, and its mineral composition was analyzed by XRD using X'Pert3 diffractometer Panalytical at the Geological Survey of Israel.

4.2. Magnetic Properties

AF (alternating field) demagnetization curves and Vibrating Sample Magnetometer (VSM) hysteresis loops were conducted for representative samples from each area. In order to assess the coercivity, AF demagnetization curves were measured after an initial pulse of 1 Tesla using ASC IM-10-30 Pulse Magnetizer. The AF was acquired starting with 5 mT steps using AF demagnetizer/magnetizer LDA-3/AMU-1, and the moment was measured using JR-6A spinner magnetometer (AGICO Inc.) at the Geological Survey of Israel. To infer the proportions and grain sizes of ferromagnetic minerals and to measure the susceptibility at high magnetic fields, hysteresis loops were produced by using Princeton Measurements Vibrating Sample Magnetometer (VSM) at the Institute for Rock Magnetism (IRM), at the University of Minnesota. To increase the accuracy, the sample holder was separately measured and then subtracted, and runs were set for a high averaging time (0.8 s) and eight repetitions.

4.3. Magnetic Fabrics

The RT-AMS was measured at a magnetic field of 700 A/m (peak field), which was found to be more accurate, and a frequency of 976 Hz, using MFK1-A Kappabridge (AGICO Inc.) at the Institute of Earth Sciences at the Hebrew University of Jerusalem. The AMS principal axes and their 95% confidence ellipses were calculated by a bootstrapping method (1,000 replicates), using the software package *Orient* 3.6.3 (Vollmer, 2016). Mean susceptibility ($k_m = k_1 + k_2 + k_3/3$), corrected degree of anisotropy ($Pj = \exp\sqrt{2\sum(\ln k_i - \ln k_m)^2}$; $i = 1$ to 3), shape of the AMS ($T = 2\ln(k_2/k_3)/\ln(k_1/k_3) - 1$), magnetic foliation ($F = k_2/k_3$), and magnetic lineation ($L = k_2/k_3$) were calculated according to Jelinek (1981).

LT-AMS was measured at a magnetic field of 425 A/m (peak field), which was found to be more accurate at low temperatures, and a frequency of 976 Hz, using MFK1-A Kappabridge at the Institute for Rock Magnetism (IRM), at the University of Minnesota. The LT-AMS was measured according to the procedure presented by Issachar et al. (2016). The samples were cooled in a liquid nitrogen bath for 50 min before the first measurement and for 5 min between axial and mean susceptibility measurements. The Kappabridge coil was protected with a thin silicon sheet, and the samples were wrapped with a Teflon layer to prevent ice condensation. Mean susceptibility values were corrected for liquid nitrogen absorption following Issachar et al. (2016).

The AARM was measured at the Institute for Rock Magnetism (IRM), the University of Minnesota. First, the samples were demagnetized at an AF field of 120 mT and then magnetized at an AF field of 100 mT, combined with a DC field of 50 μT, using D2000 DTech Precision Instruments AF (de)magnetizer. The applied magnetizations were measured on a 2G Enterprises (Mtn. View, CA) RF SQUID Superconducting Rock Magnetometer. For high accuracy, we used the nine positions scheme introduced by Girdler (1961). Principal directions and anisotropy were calculated by the AvARM (Anisotropy of full-vector Anhysteretic Remanent Magnetization) method using the three components of each vector (Bilardello & Jackson, 2014).

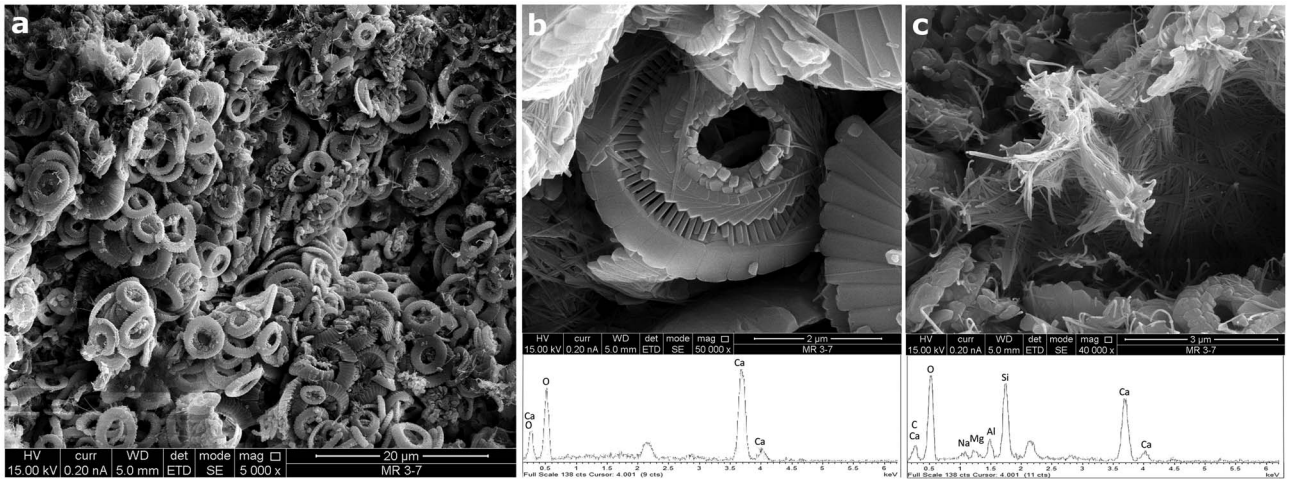

Figure 3. Extrahigh-resolution SEM images and associated EDS spectra of Eocene chalk sample. (a) Well-preserved coccoliths forming the matrix of the chalk. (b) Zoom in on a coccolith exclusively builds of calcite and embedded fibrous clays in the background. (c) A cluster of fibrous clays (palygorskite) forming a woven fabric texture.

5. Results

5.1. Petrography, Mineralogy, and Geochemistry

Figure 3 shows SEM images and the associated EDS analysis of a representative sample. The rock matrix is composed of well-preserved coccoliths and fibrous clays, commonly clustered, and form woven texture (Figure 3c) known as "mountain leather" (Esquivel et al., 2005). Voids are common in between (Figure 3a).

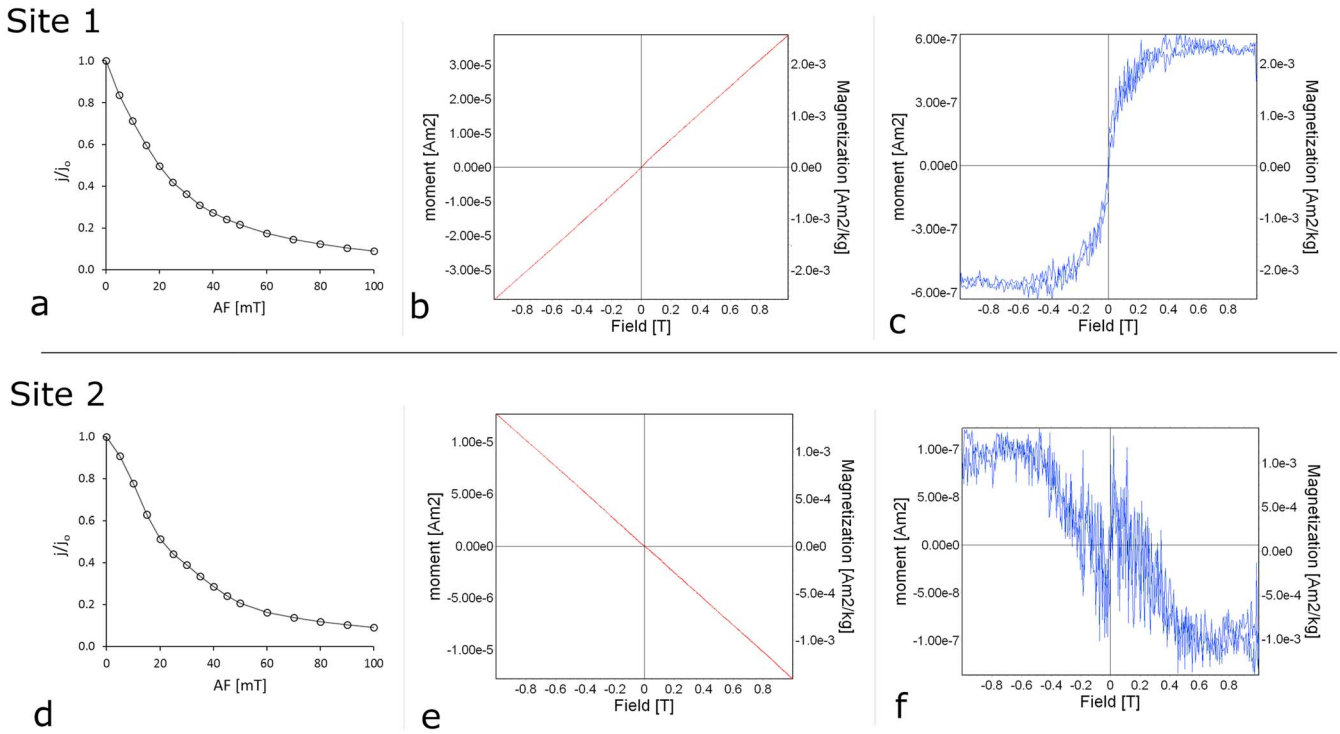

Figure 4. Magnetic properties of two representative chalk samples. (a) AF demagnetization curve indicating that the remanent magnetization is carried by low-coercivity minerals. (b) VSM raw data showing paramagnetic dominancy and negligible ferromagnetic effect. (c) Slope-corrected VSM showing noisy ferromagnetic effect. (d) AF demagnetization curve indicating that the remanent magnetization is carried by low-coercivity minerals. (e) VSM raw data showing diamagnetic dominancy and negligible ferromagnetic effect. (f) Slope-corrected VSM showing noisy ferromagnetic effect.

Table 1
Data of RT-AMS, LT-AMS, and Separated Diamagnetic Fabrics

	RT-AMS					LT-AMS					Separated diamagnetic				
Sample	k_m [$\times 10^{-6}$ SI]	*T*	*Pj*	*L*	*F*	k_m [$\times 10^{-6}$ SI]	*T*	*Pj*	*L*	*F*	k_m [$\times 10^{-6}$ SI]	*T*	*Pj*	*L*	*F*
Site 1-1	0.99	−0.64	1.060	1.049	1.011	36.19	0.89	1.003	1.000	1.003	−12.87	−0.14	1.005	1.003	1.002
Site 1-2	1.47	−0.16	1.065	1.037	1.027	36.19	0.34	1.004	1.001	1.003	−12.87	−0.24	1.007	1.004	1.003
Site 1-3	1.01	−0.15	1.141	1.077	1.060	-	-	-	-	-	−12.87	0.38	1.009	1.003	1.006
Site 1-4	1.50	−0.91	1.058	1.055	1.002	-	-	-	-	-	−12.87	0.14	1.008	1.003	1.004
Site 1-5	1.28	−0.25	1.039	1.024	1.015	-	-	-	-	-	−12.87	−0.88	1.004	1.004	1.000
Site 1-6	1.33	0.13	1.052	1.022	1.030	-	-	-	-	-	−12.87	−0.57	1.006	1.004	1.001
Site 1-7	1.32	−0.09	1.055	1.029	1.025	-	-	-	-	-	−12.87	0.08	1.006	1.003	1.003
Site 1-8	1.71	−0.39	1.067	1.046	1.020	-	-	-	-	-	−12.87	0.45	1.007	1.002	1.005
Site 1-9	2.06	−0.59	1.034	1.027	1.007	43.99	0.48	1.003	1.001	1.002	−12.87	−0.03	1.006	1.003	1.003
Site 1-10	3.61	0.26	1.019	1.007	1.012	-	-	-	-	-	−12.87	−0.27	1.007	1.004	1.002
Site 1-11	0.88	0.24	1.084	1.030	1.052	48.66	0.47	1.003	1.001	1.002	−12.87	0.52	1.003	1.001	1.003
Site 1-12	4.21	0.08	1.020	1.009	1.011	-	-	-	-	-	−12.87	0.13	1.006	1.003	1.004
Site 1-13	3.73	−0.05	1.025	1.013	1.012	47.05	0.83	1.003	1.000	1.003	−12.87	0.49	1.007	1.002	1.005
Site 2-1	7.76	0.70	1.009	1.001	1.008	-	-	-	-	-	−12.87	−0.41	1.003	1.002	1.001
Site 2-2	8.13	0.75	1.011	1.001	1.009	-	-	-	-	-	−12.87	0.28	1.003	1.001	1.002
Site 2-3	10.21	0.73	1.007	1.001	1.006	-	-	-	-	-	−12.87	0.60	1.002	1.000	1.001
Site 2-4	11.09	0.64	1.006	1.001	1.005	69.45	0.31	1.004	1.001	1.003	−12.87	0.63	1.003	1.001	1.002
Site 2-5	8.89	0.34	1.009	1.003	1.006	-	-	-	-	-	−12.87	−0.33	1.002	1.001	1.001
Site 2-6	8.86	−0.24	1.010	1.006	1.004	-	-	-	-	-	−12.87	−0.35	1.004	1.003	1.001
Site 2-7	10.15	0.64	1.008	1.001	1.006	-	-	-	-	-	−12.87	−0.07	1.005	1.002	1.002
Site 2-8	11.55	0.66	1.007	1.001	1.006	80.86	0.64	1.003	1.001	1.003	−12.87	−0.38	1.003	1.002	1.001
Site 2-9	10.93	−0.22	1.006	1.003	1.002	69.18	-	-	-	-	−12.87	0.31	1.005	1.002	1.003
Site 2-10	8.17	−0.25	1.014	1.009	1.005	58.09	-	-	-	-	−12.87	0.37	1.006	1.002	1.004
Site 2-11	8.48	0.47	1.011	1.003	1.008	67.67	0.61	1.003	1.001	1.003	−12.87	−0.15	1.005	1.003	1.002
Site 2-13	12.32	0.01	1.009	1.004	1.004	-	-	-	-	-	−12.87	−0.29	1.005	1.003	1.002
Site 2-14	9.15	0.40	1.008	1.002	1.006	-	-	-	-	-	−12.87	−0.69	1.003	1.002	1.000
Site 2-15	9.19	−0.36	1.007	1.004	1.002	-	-	-	-	-	−12.87	−0.26	1.004	1.002	1.001
Site 2-16	7.67	0.27	1.011	1.004	1.007	-	-	-	-	-	−12.87	0.03	1.002	1.001	1.001
Site 2-17	8.04	0.71	1.007	1.001	1.006	-	-	-	-	-	−12.87	−0.22	1.002	1.001	1.001
Site 2-18	4.66	−0.11	1.019	1.010	1.008	-	-	-	-	-	−12.87	0.49	1.004	1.001	1.003
Site 2-19	5.25	0.45	1.015	1.004	1.011	-	-	-	-	-	−12.87	0.43	1.004	1.001	1.003
Site 2-20	7.69	0.21	1.014	1.005	1.008	-	-	-	-	-	−12.87	0.46	1.004	1.001	1.003
Site 2-21	6.83	0.67	1.014	1.002	1.012	-	-	-	-	-	−12.87	−0.73	1.004	1.004	1.001
Site 3-3	−3.02	0.35	1.018	1.006	1.012	-	-	-	-	-	−12.87	−0.55	1.009	1.007	1.002
Site 3-4	−3.87	0.14	1.014	1.006	1.008	-	-	-	-	-	−12.87	−0.40	1.008	1.006	1.002
Site 3-5	−4.73	0.27	1.013	1.005	1.008	12.46	0.80	1.002	1.000	1.002	−12.87	−0.44	1.008	1.006	1.002
Site 3-6	1.97	−0.55	1.024	1.018	1.005	39.67	0.32	1.006	1.002	1.004	−12.87	−0.51	1.013	1.010	1.003
Site 3-7	−2.86	−0.02	1.016	1.008	1.008	21.09	0.06	1.017	1.008	1.009	−12.87	−0.26	1.010	1.007	1.004
Site 3-8	−2.84	0.15	1.023	1.010	1.013	19.28	0.46	1.003	1.001	1.002	−12.87	−0.39	1.010	1.007	1.003
Site 3-9	−4.68	0.46	1.012	1.003	1.009	14.26	−0.32	1.033	1.022	1.011	−12.87	−0.42	1.010	1.007	1.003
Site 3-13	−1.79	−0.12	1.017	1.009	1.007	-	-	-	-	-	−12.87	−0.34	1.009	1.006	1.003
Site 3-14	−3.41	0.10	1.018	1.008	1.010	-	-	-	-	-	−12.87	−0.83	1.009	1.008	1.001

Note. k_m is mean susceptibility, *T* is shape of anisotropy, *Pj* is corrected anisotropy degree, *L* is magnetic lineation, and *F* is magnetic foliation.

No impurities were detected in the coccoliths by the EDS analysis (Figure 3b). The clay elemental composition includes Si, Al, Na, and Mg and agrees with XRD observations of palygorskite and smectite. Fe content in the bulk samples is 4,000 ± 10% ppm and in the carbonate fraction only 125 ± 25% ppm. The average I.R. fraction in the representative samples is 6% (weight) and about half of it is clay minerals, hence, ~3% of the rock mass. The other 3% are mainly quartz and opal.

5.2. Magnetic Properties

Figure 4 shows the main results of the magnetic tests. The AF demagnetization curves (Figures 4a and 4d) indicate that most of the magnetic moment (up to 90%) is lost by a demagnetization field of 90 mT, suggesting that mostly low-coercivity minerals carry the remanent magnetization. The raw data of the VSM indicate a paramagnetic dominancy in the Site 1 and Site 2 samples and a diamagnetic dominancy in the Site 3 sample (Figures 4b and 4e). The ferromagnetic effect is negligible, as evident in the noisy slope corrected curves (Figures 4c and 4f).

5.3. Magnetic Fabrics

Tables 1 and 2 summarize the values of the anisotropy parameters of RT-AMS, LT-AMS, AARM, and the separated diamagnetic fabric. Notably, the anisotropy parameters, *Pj*, *L*, and *F* of RT-AMS are very high compared

Table 2
Data of AARM Fabrics

Sample	k_r[×10^{-6} SI]	T	Pj	L	F
Site 1–1	2.22	−0.03	1.0.98	1.049	1.047
Site 1–2	2.20	0.52	1.078	1.017	1.056
Site 1–9	2.23	0.19	1.142	1.055	1.082
Site 1–13	2.24	0.35	1.151	1.046	1.098
Site 2–4	19.65	−0.50	1.175	1.123	1.040
Site 2–5	18.45	−0.10	1.096	1.052	1.042
Site 2–6	19.34	−0.06	1.132	1.068	1.060
Site 2–7	21.21	0.65	1.082	1.013	1.063
Site 2–8	26.88	−0.13	1.099	1.055	1.042
Site 2–9	28.41	−0.48	1.055	1.039	1.014
Site 2–10	23.46	−0.31	1.111	1.070	1.036
Site 2–11	22.15	0.80	1.119	1.010	1.096
Site 3–5	3.91	−0.19	1.069	1.040	1.027
Site 3–6	8.01	0.67	1.110	1.016	1.085
Site 3–8	7.06	0.15	1.140	1.056	1.077
Site 3–9	4.48	−0.01	1.122	1.060	1.059

Note. k_r is mean remanence susceptibility, *T* is shape of anisotropy, *Pj* is corrected anisotropy degree, *L* is magnetic lineation, and *F* is magnetic foliation.

to their values in LT-AMS and in the separated diamagnetic fabrics of Site 1 and Site 3. This phenomenon could be explained by the low values of $k_m \sim 0$, which leads to an asymptotic increase of the anisotropy parameters (Hrouda, 2004). RT-AMS and LT-AMS were measured at fields of 700 A/m and 425 A/m (peak fields), respectively. These fields were chosen for best measurement accuracy. In RT-AMS, a high field (700 A/m) had a better signal-to-noise ratio, since the signal of the samples was very weak. At low temperatures, we encountered instrumental difficulties to apply the field of 700 A/m, and, therefore, the LT-AMS was measured at 425 A/m. Ferromagnetic susceptibilities and their grain distribution might be different at different fields. Nevertheless, this effect is not expected to be significant in the present samples, since the ferromagnetic contribution to the AMS is negligible, as is further explained below. The k_m^{RT} values of the Site 1 samples range between 0.9 and 4.2×10^{-6} SI, while k_m^{LT} range between 36.2 and 48.7×10^{-6} SI. For Site 2, k_m^{RT} values range between 6.8 and 12.3×10^{-6} SI, while k_m^{LT} range between 58.1 and 80.8×10^{-6} SI. For Site 3, k_m^{RT} values range between -4.7 and 2.0×10^{-6} SI, while k_m^{LT} range between 12.5 and 39.7×10^{-6} SI. Figure 5a shows k_m^{LT} versus k_m^{RT}. The positive linear correlation with $R^2 = 0.98$ suggests that the increase in the susceptibility is related to increase in the paramagnetic contents, whereas diamagnetic and ferromagnetic contents in the samples are almost constant (see section 2 and Figure 1). The linear regression slope of 3.75 ± 0.15 reveals the paramagnetic amplification factor (α). This value is within the error of the expected amplification factor for LT-AMS measurements in air (Issachar et al., 2016). In addition, the linear regression suggests that $k_m^{LT} = k_m^{RT}$ for -11.2×10^{-6} SI

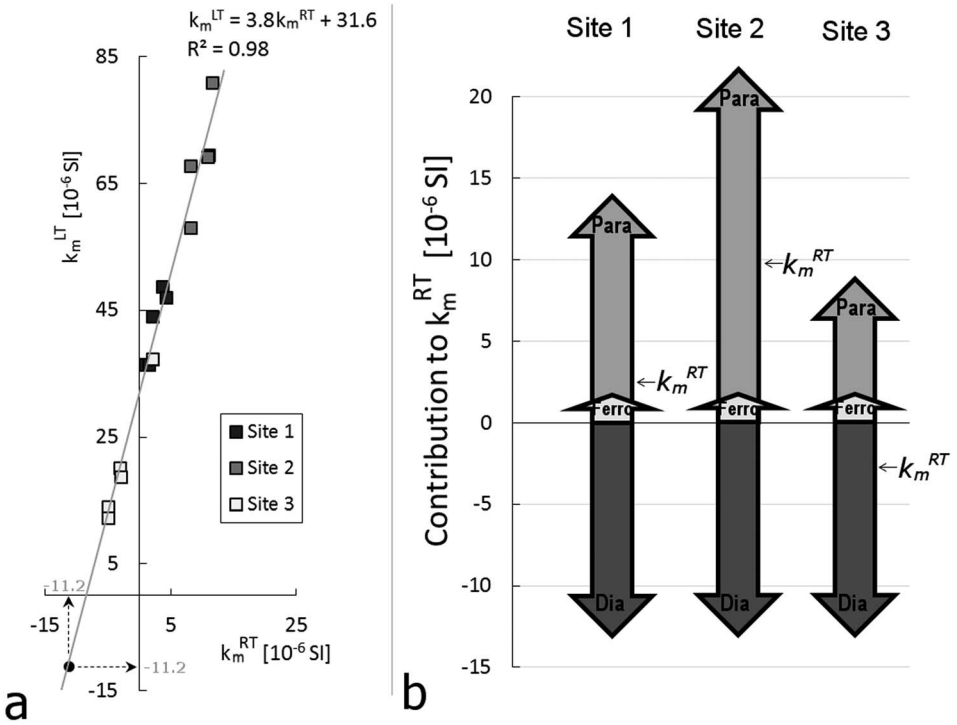

Figure 5. (a) Low-temperature mean susceptibility (k_m^{LT}) versus room temperature mean susceptibility (k_m^{RT}) showing linear correlation. The slope of the linear regression is $\alpha = 3.75 \pm 0.15$. LT and RT susceptibilities are equal to -11.2×10^{-6} SI. (b) Calculated average diamagnetic, paramagnetic, and ferromagnetic contributions to k_m^{RT}.

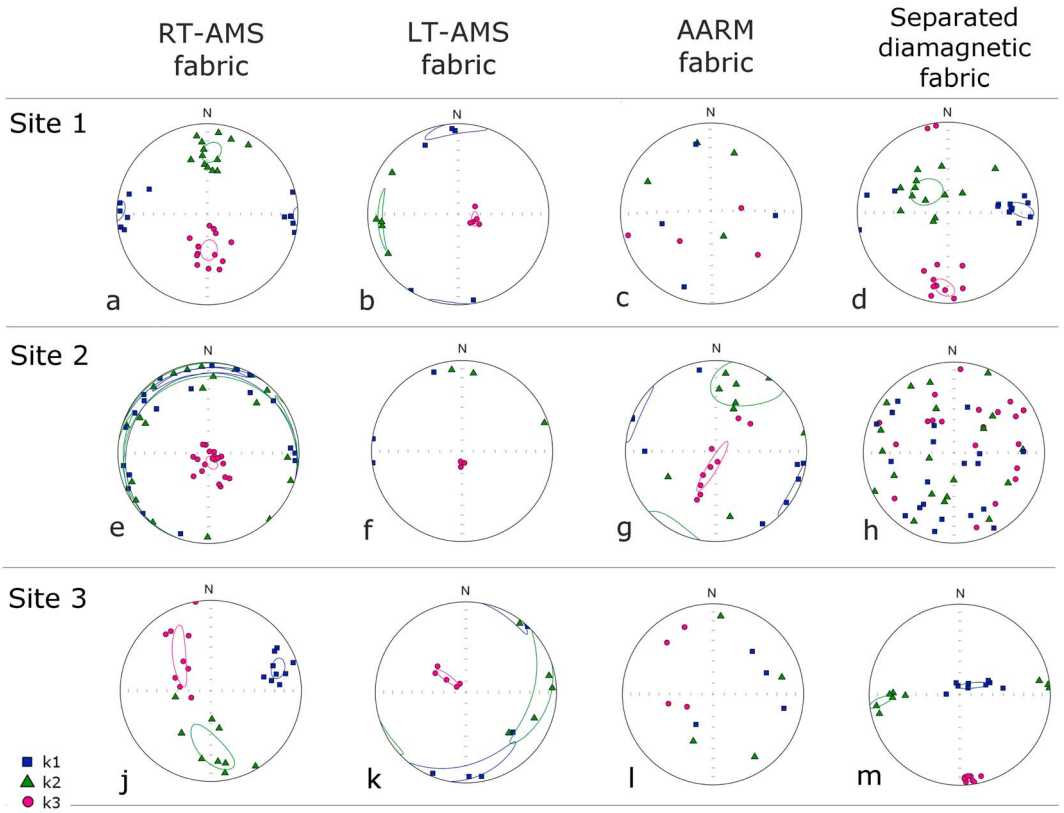

Figure 6. Lower hemisphere, equal-area projection of bootstrapping principal axes (95% confidence cones; 1,000 replicates) of RT-AMS, LT-AMS, AARM, and separated diamagnetic fabrics of Site 1, Site 2, and Site 3 chalk samples. The $\boldsymbol{k_1}$, $\boldsymbol{k_2}$, and $\boldsymbol{k_3}$ axes are marked by solid squares (blue), triangles (green), and circles (pink), respectively.

(Figure 5a), which is close to the susceptibility of a single calcite crystal (-12.87×10^{-6} SI) (Nye, 1957). The average diamagnetic, paramagnetic, and ferromagnetic contribution to $k_m{}^{RT}$ were calculated based on equations (5) and (6). In Site 1 the contributions were -12×10^{-6} SI, 13×10^{-6} SI, and 1.7×10^{-6} SI, respectively; in Site 2 the contributions were -12×10^{-6} SI, 21×10^{-6} SI, and 1.7×10^{-6} SI, respectively; and in Site 3 the contributions were -12×10^{-6} SI, 9×10^{-6} SI, and 1.7×10^{-6} SI, respectively (Figure 5b).

Based on equation (7), the separation of the diamagnetic fabric was solved for each of the samples. The mean susceptibility (k_{md}) was set to the value of calcite ($k_m = -12.87 \times 10^{-6}$ SI), whereas k_{mp} and k_{mf} were estimated from the linear regression of $k_m{}^{LT}$ versus $k_m{}^{RT}$ (equations (5) and (6)). The normalized mean LT-AMS and AARM tensors were used as $\widehat{\boldsymbol{k_p}}$ and $\widehat{\boldsymbol{k_f}}$, respectively. The results of the separation procedure suggest that the ferromagnetic component has no significant influence and therefore can be neglected. Figure 6 and Table 3 present the orientation of the principal axes and 95% confidence ellipses of RT-AMS, LT-AMS, AARM, and separated diamagnetic fabric. The RT-AMS fabric of Site 1 (Figure 6a) shows clusters of $\boldsymbol{k_1}$, $\boldsymbol{k_2}$, and $\boldsymbol{k_3}$ axes. LT-AMS fabric (Figure 6b) shows subvertical $\boldsymbol{k_3}$ axes and a subhorizontal griddle of $\boldsymbol{k_1}$ and $\boldsymbol{k_2}$ axes. The AARM results indicate an inconclusive fabric (Figure 6c). The separated diamagnetic fabric shows clusters of all three AMS axes (Figure 6d). For Site 2, the RT-AMS fabric (Figure 6e) shows subvertical $\boldsymbol{k_3}$ axes and a subhorizontal griddle of $\boldsymbol{k_1}$ and $\boldsymbol{k_2}$ axes. The LT-AMS fabric (Figure 6f) shows subvertical $\boldsymbol{k_3}$ axes and a subhorizontal griddle of $\boldsymbol{k_1}$ and $\boldsymbol{k_2}$ axes. The AARM results indicate weak clusters of all principal axes with subvertical $\boldsymbol{k_3}$ and subhorizontal $\boldsymbol{k_1}$ and $\boldsymbol{k_2}$ axes (Figure 6g). The separated diamagnetic fabric indicates an inconclusive fabric (Figure 6h). For Site 3, the RT-AMS fabric (Figure 6j) shows clustered $\boldsymbol{k_1}$ axes and weak foliation of $\boldsymbol{k_2}$ and $\boldsymbol{k_3}$ axes. The LT-AMS fabric (Figure 6k) shows subvertical $\boldsymbol{k_3}$ axes and a subhorizontal griddle of $\boldsymbol{k_1}$ and $\boldsymbol{k_2}$ axes. The AARM results indicate an inconclusive fabric (Figure 6l). The separated diamagnetic fabric shows clusters of all three AMS axes (Figure 6m).

Table 3
Mean Tensor Principal Orientations and Their 95% Bootstrap Confidence Cones Calculated With 1,000 Replicates

		RT-AMS		Lt-AMS		AARM		Separated diamagnetic	
Site		Principal axes trend/plunge	95% confidence angles max/min	Principal axes trend/plunge	95% confidence angles max/min	Principal axes trend/plunge	95% confidence angles max/min	Principal axes trend/plunge	95% confidence angles max/min
Site 1	k_1	272/02	09/06	357/05	23/07	-	-	088/20	13/05
	k_2	003/32	11/07	266/15	20/03	-	-	314/63	14/12
	k_3	178/57	10/08	106/74	06/03	-	-	183/18	10/06
Site 2	k_1	262/02	06/82	284/02	-	115/00	21/07	-	-
	k_2	356/08	08/87	015/12	-	022/19	30/23	-	-
	k_3	161/81	06/04	180/78	-	194/74	27/04	-	-
Site 3	k_1	072/23	09/06	184/09	45/07	-	-	056/75	13/02
	k_2	178/34	29/10	090/15	46/10	-	-	265/13	14/02
	k_3	317/47	29/06	307/68	12/03	-	-	173/07	03/02

Note. Numbers are in degrees. k_1, k_2, and k_3 are maximum, intermediate, and minimum principal susceptibilities eigenvectors, respectively.

6. Discussion

6.1. Carriers of the AMS

The studied chalk rocks consist of diamagnetic, paramagnetic, and ferromagnetic fabrics. Coccolith calcite, composing ~95% of the rock mass, constitutes the diamagnetic fabric. The average Fe content in the carbonate fraction is significantly lower than the threshold of 400 ppm that may produce inverse AMS fabric and paramagnetic behavior (Schmidt, Gunther, & Hirt, 2006), indicating that the calcite can be considered purely diamagnetic. This is in accordance with the setting of k_{md} to the susceptibility value of pure calcite. Fibrous clays, palygorskite and smectite, compose ~3% of the rock mass and constitute the paramagnetic fabric. Fe oxides that constitute the ferromagnetic fabric are very rare in the samples. Ferromagnetic minerals have a low coercivity, suggesting that standard AARM schemes reflect the ferromagnetic susceptibility tensor (Bilardello & Jackson, 2014). For ferromagnetic grains, the AMS and AARM might not reflect the same magnetic fabrics (Hrouda, Henry, & Borradaile, 2000). However, according to the AARM fabrics, this effect is not significant in the present samples (Figures 5 and 6). The separation procedure reveals that the diamagnetic and paramagnetic susceptibilities in the three sites cancel each other, resulting in slightly positive mean susceptibility in Site 1 and Site 2 and slightly negative mean susceptibility in Site 3 (Figure 5). This means that the RT-AMS of these sites represents a composite fabric, reflecting the competing effects of diamagnetic and paramagnetic fabrics. Figure 6 shows that for Site 1 and Site 3, k_3 axes of RT-AMS are oriented in between LT-AMS and the clustered separated diamagnetic k_3 axes. Hence, the separation of the diamagnetic and paramagnetic fabrics is necessary for reliable interpretation of the magnetic fabrics.

The separation procedure enables us to examine how the RT-AMS fabric changes for different paramagnetic contributions, namely, for increasing and decreasing k_{mp} values (equation (1)). Figure 7 shows k_m^{RT} as a function of the increase in k_{mp}. By calculating the AMS fabrics based on the LT-AMS and the isolated diamagnetic fabric for 5% k_{mp} increments, we infer susceptibility values for which diamagnetic and paramagnetic fabrics dominate the RT-AMS. The analysis shows that for up to 35% of paramagnetic contribution (comparable to $k_m^{RT} = -6 \times 10^{-6}$ SI), the diamagnetic fabric dominates the RT-AMS. For 65% of paramagnetic contribution (comparable to $k_m^{RT} = 11 \times 10^{-6}$ SI) and above, the paramagnetic fabric dominates the RT-AMS. In the zone of 35% to 65% paramagnetic contribution (comparable to $k_m^{RT} = -6$ to 11×10^{-6} SI), the AMS shows composite fabrics. In this zone, the separation of diamagnetic and paramagnetic fabrics is essential for reliable interpretation. The analysis preformed above is general and applicable to all carbonate rocks in which ferromagnetic contribution is negligible. In the current study, the chalks of both sites show k_m^{RT} values in the composite zone, indicating that applying the separation procedure is required.

6.2. The Origin of the Magnetic Fabrics

The results of the present study suggest that both diamagnetic and paramagnetic fabrics are anisotropic in Site 1 and Site 3 while in Site 2, the diamagnetic fabric is isotropic. The LT-AMS, which is comparable with the paramagnetic fabric, indicates that the clays preserve their sedimentary origin, as k_3 axes are bed normal, and k_1 and k_2 axes form horizontal foliation (Figures 6b, 6f, and 6k). The shape of the paramagnetic fabric is

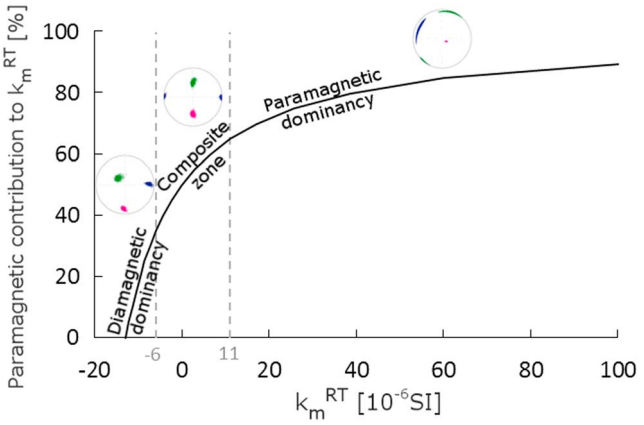

Figure 7. Modeled AMS fabrics for different paramagnetic contributions. The *x* axis represents the room temperature mean susceptibility, and the *y* axis represents the paramagnetic contribution (%) to the room temperature mean susceptibility. Stereoplots are lower hemisphere, equal-area projections of AMS bootstrapping principal axes (1,000 replicates) with k_1 (blue), k_2 (green), and k_3 (pink). Zones of diamagnetic and paramagnetic dominancy and composite zone in between are marked with vertical dash lines.

oblate (Figure 8), which is common for depositional and compaction processes in clays (Aubourg et al., 2004; Oertel, 1983; Parés, van der Pluijm, & Dinares-Turell, 1999).

The shape of the separated diamagnetic fabrics is prolate to neutral (Figure 8), with horizontal approximately N-S trending $\boldsymbol{k_3}$ axes (Figures 6d and 6m) in Site 1 and Site 3. Previous studies show that calcite-bearing rocks are sensitive to strain and tend to develop prolate AMS fabric with $\boldsymbol{k_3}$ axes parallel to the maximum shortening direction (Almqvist et al., 2011; Borradaile, Almqvist, & Geneviciene, 2012; de Wall et al., 2000; Levi & Weinberger, 2011; Owens & Rutter, 1978). Furthermore, comparison with direct texture techniques shows that the AMS in these rocks is controlled by the crystallography of calcite and reflects a preferred orientation of *c axes* parallel to $\boldsymbol{k_3}$ axes (de Wall et al., 2000; Owens & Rutter, 1978; Schmidt et al., 2009). Preferred orientation in calcite rocks is commonly developed by mechanisms of intercrystal deformation, that is, twining, grain boundary sliding, and dislocation glide (Evans et al., 2003). While intercrystal deformation may control the diamagnetic fabrics in the studied chalks, another mechanism of coccolith rotation could be considered. SEM images indicate that the chalks consist of well-preserved, disk-shaped calcite coccoliths of ~4 μm diameter (Figure 3b). Morphological studies infer that the crystals in coccoliths are built as an assembly of a ring of single crystals with alternating subvertical and subradial *c axes* orientations (Saruwatari et al., 2006; Young et al., 1992). Thus, a single coccolith has an overall preferred crystallographic orientation that is subperpendicular to its plate. Under shear strain, the coccoliths may slide and rotate. This slippage and rotation of the coccoliths would lead to the development of preferred crystallographic orientation in the rock parallel to the maximum shortening direction (Figure 9). This mechanism is analog to the development of AMS in phyllosilicates (Parés, 2015). Moreover, the mechanism of coccolith rotation can act simultaneously with the mechanisms of intercrystal deformation and intensify the diamagnetic fabric, as both respond to strain in a similar manner.

The orientation of the AMS axes in the separated diamagnetic fabric of Site 1 and Site 3 indicates a tectonic origin, as $\boldsymbol{k_3}$ axes are horizontally oriented. This suggests that the diamagnetic fabric in chalks is more sensitive to tectonic strain than the paramagnetic fabric, which preserves the depositional fabric.

6.3. Strain Field Around the DSF

The left-lateral motion along the DSF is associated with a regional strain field with NNW-SSE oriented S_{Hmax}, as indicated by mesostructure analysis (Eyal, 1996; Eyal & Reches, 1983). Garfunkel (1981) predicted S_{Hmax} to be deflected locally next to strands of the DSF. According to Garfunkel (1981, 2014), along the southern segment (southern of ca. lat. 33°), S_{Hmax} trends approximately N-S, parallel to approximately N-S strands of the DSF. This segment is characterized as transtensional, with a wide topographic depression controlled by pull-apart structures. In contrast, in the northern segment (north of ca. lat. 33°) the S_{Hmax} trends approximately W-E, normal to approximately N-S strands of the DSF. This area is dominated by transpression, pronounced by intensive contractional deformation (folds and thrusts), perpendicular to the general strike of the DSF (Weinberger, 2014).

The diamagnetic fabrics of Site 1 and Site 3 obtained in this study suggest an approximately N-S direction of $\boldsymbol{k_3}$ axes that approximates the S_{Hmax} directions at both sites. This indicates a deflection from the regional S_{Hmax}, in agreement with recent studies near Rosh-Pinna (Issachar et al., 2015) and Metulla (Levi & Weinberger, 2011; Weinberger, 2014; Weinberger, Gross, & Sneh, 2009). In the Rosh-Pinna area, north of the

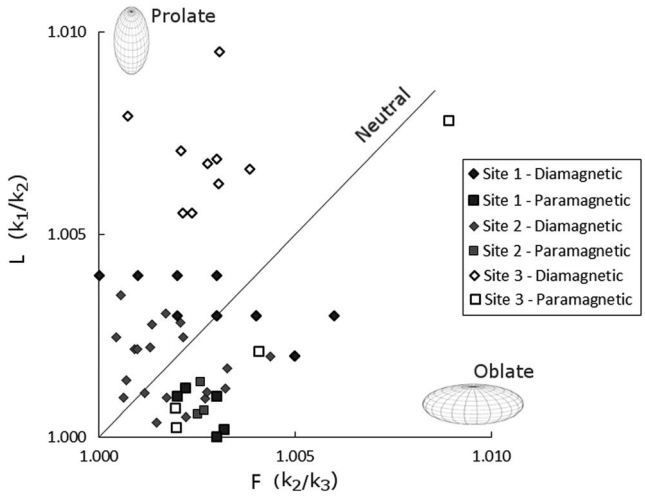

Figure 8. L-F plot for diamagnetic (diamonds) and paramagnetic (squares) fabrics. The diamagnetic fabric shows more of a prolate shape, and the paramagnetic fabric shows more of an oblate shape.

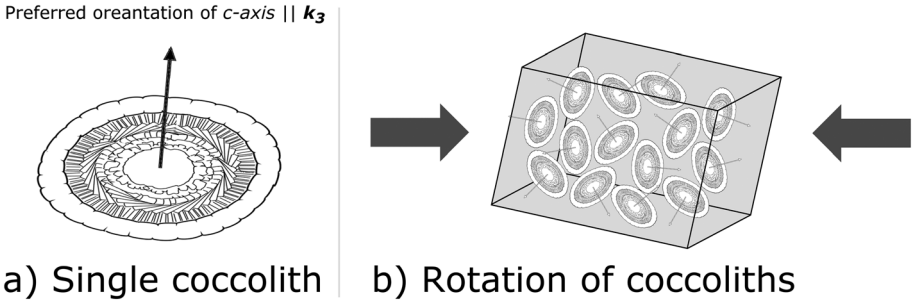

Figure 9. (a) Preferred orientation of calcite crystals in a single coccolith oriented vertically to the coccolith plane. (b) Mechanism of coccolith rotation leads to the development of preferred crystallographic orientation in the rock parallel to the maximum shortening direction (S_{Hmax}).

Sea of Galilee, magnetic fabrics and structural studies revealed an approximately N-S S_{Hmax} close to the DSF. In the Metulla area, farther north of the Rosh-Pinna area, magnetic fabrics and structural analyses reveal an approximately E-W S_{Hmax} close to the DSF. All these results corroborate Garfunkel (2014). The diamagnetic fabric of Site 2, which is located 8 km east of the DSF (Figure 1b), indicates an isotropic fabric. This suggests that the width of the deformation zone east of this sector of the DSF, as reflected by the diamagnetic fabrics, is <8 km. We therefore suggest that magnetic fabrics of carbonate rocks along plate boundaries provide a reliable strain indicator and are useful for tectonic and structural studies.

7. Conclusions

1. The studied chalks contain a pure diamagnetic carbonate coccolith matrix, paramagnetic clays (palygorskite and smectite), and minor quantities of low-coercivity ferromagnetic Fe minerals.
2. The diamagnetic fabric can be separated analytically by subtracting the paramagnetic and ferromagnetic fabrics from the bulk RT-AMS, using RT-AMS, LT-AMS, and AARM measurements.
3. The separation indicates that differences of the mean susceptibility values (k_m^{RT}) in the chalk samples are related to differences in the paramagnetic contents.
4. The RT-AMS shows a composite fabric of diamagnetic and paramagnetic fabrics.
5. Our analyses indicate that in the case of chalks, where the ferromagnetic contribution is negligible, the diamagnetic fabric is expected to dominate the RT-AMS for mean susceptibilities $<-6\times10^{-6}$ SI, whereas the paramagnetic fabric is dominant for mean susceptibilities $>11\times10^{-6}$ SI. For mean susceptibilities that range between -6 and 11×10^{-6} SI, a composite RT-AMS fabric is expected.
6. The studied chalks indicate that the paramagnetic fabric preserves the original depositional fabric, while the diamagnetic fabric has a tectonic origin. Thus, in chalks, the diamagnetic fabric is more sensitive to tectonic strain than the paramagnetic fabric.
7. We suggest that under shear strain, a mechanism of coccolith rotation can act simultaneously with mechanisms of intercrystal deformation, leading to the development of a preferred crystallographic orientation in the rock. This contributes to the acquisition of the AMS with $\boldsymbol{k_3}$ axes parallel to the maximum shortening direction.
8. The maximum horizontal shortening direction at the studied areas is approximately N-S, suggesting a deflection of the strain field adjacent to strands of the DSF.

Acknowledgments
This study was supported by grants from the Israel Science Foundation 1245/11 and 868/17 to R. W., the Israel Science Foundation Center of Excellence grant 1436/14 to S. M., and the Israeli Ministry of Energy and the Naomi Foundation through the Tel Aviv University GRTF Program. The Institute for Rock Magnetism is funded by the NSF Instruments and Facilities program and by the University of Minnesota. We wish to thank the IRM for hosting and supporting RI during the course of this study; especially, we wish to thank Andrea Biedermann, Dario Bilardello, and Mike Jackson for fruitful discussions and help. We thank Ron Shaar and Yael Ebert for their kind collaboration and help and Yehudit Harlavan for her help in analyzing the geochemical data. The field assistance of Daniel Zvi, Ran Benyamin, Asaf Ido, Iyad Swaed, Oria Vanunu, and Misha Kitin is highly acknowledged. We are grateful to the Editor of JGR, Paul Tregoning, and to Jessica Till and an anonymous reviewer for their helpful reviews that improved this paper. All the data used for this study is accessible by contacting the authors at ranissachar@gmail.com and available online at https://figshare.com.

References

Almqvist, B. S. G., Hirt, A. M., Herwegh, M., & Leiss, B. (2011). Magnetic anisotropy reveals Neogene tectonic overprint in highly strained carbonate mylonites from the Morcles nappe, Switzerland. *Journal of Structural Geology*, *33*(5), 1010–1022. https://doi.org/10.1016/j.jsg.2011.02.002

Aubourg, C., Smith, B., Bakhtari, H., Guya, N., Eshragi, A., Lallemant, S., et al. (2004). Post-Miocene shortening pictured by magnetic fabric across the Zagros-Makran syntaxis (Iran). *Geological Society of America, Special Paper*, *383*, 17–40.

Benjamini, C. (1984). Stratigraphy of the Eocene of the Arava Valley (eastern and southern Negev, southern Israel). *Israel Journal of Earth Sciences*, *33*, 167–177.

Bilardello, D., & Jackson, M. (2014). A comparative study of magnetic anisotropy measurement techniques in relation to rock-magnetic properties. *Tectonophysics*, *629*, 39–54. https://doi.org/10.1016/j.tecto.2014.01.026

Borradaile, G. J. (1988). Magnetic-susceptibility, petrofabrics and strain. *Tectonophysics*, *156*(1-2), 1–20. https://doi.org/10.1016/0040-1951(88)90279-x

Borradaile, G. J. (1991). Correlation of strain with anisotropy of magnetic-susceptibility (AMS). *Pure and Applied Geophysics*, *135*(1), 15–29. https://doi.org/10.1007/bf00877006

Borradaile, G. J., Almqvist, B. S. G., & Geneviciene, I. (2012). Anisotropy of magnetic susceptibility (AMS) and diamagnetic fabrics in the Durness Limestone, NW Scotland. *Journal of Structural Geology*, *34*, 54–60. https://doi.org/10.1016/j.jsg.2011.10.008

Borradaile, G. J., Fralick, P. W., & Lagroix, F. (1999). Acquisition of anhysteretic remanence and tensor subtraction from AMS isolates true palaeocurrent grain alignments. *Geological Society of London, Special Publication*, *151*(1), 139–145. https://doi.org/10.1144/GSL.SP.1999.151.01.14

Borradaile, G. J., & Henry, B. (1997). Tectonic applications of magnetic susceptibility and its anisotropy. *Earth-Science Reviews*, *42*(1-2), 49–93. https://doi.org/10.1016/S0012-8252(96)00044-X

Borradaile, G. J., & Jackson, M. (2010). Structural geology, petrofabrics and magnetic fabrics (AMS, AARM, AIRM). *Journal of Structural Geology*, *32*(10), 1519–1551. https://doi.org/10.1016/j.jsg.2009.09.006

Borradaile, G. J., Lagroix, F., Hamilton, T. D., & Trebilcock, D. A. (2010). Ophiolite tectonics, rock magnetism and palaeomagnetism, Cyprus. *Surveys in Geophysics*, *31*(3), 285–359. https://doi.org/10.1007/s10712-009-9090-2

Braun, D., Weinberger, R., Eyal, Y., Feinstein, S., Harlavan, Y., & Levi, T. (2015). Distinctive diamagnetic fabrics in dolostones evolved at fault cores, the Dead Sea Transform. *Journal of Structural Geology*, *77*, 11–26. https://doi.org/10.1016/j.jsg.2015.05.007

Buchbinder, B., & Gvirtzman, G. (1966). *The geological map of HaShephela Area, 1:50,000*. Jerusalem: Geological Survey of Israel.

Cifelli, F., Mattei, M., Rashid, H., & Ghalamghash, J. (2013). Right-lateral transpressional tectonics along the boundary between Lut and Tabas blocks (Central Iran). *Geophysical Journal International*, *193*(3), 1153–1165. https://doi.org/10.1093/gji/ggt070

Cullity, B. D. (1972). *Introduction to magnetic materials*. Addison-Wesley, University of Notre Dame.

De Wall, H., Bestmann, M., & Ullemeyer, K. (2000). Anisotropy of diamagnetic susceptibility in Thassos marble: A comparison between measured and modeled data. *Journal of Structural Geology*, *22*(11-12), 1761–1771. https://doi.org/10.1016/s0191-8141(00)00105-x

Debacker, T., Robion, P., & Sintubin, M. (2004). *The anisotropy of magnetic susceptibility (AMS) in low-grade, cleaved pelitic rocks: Influence of cleavage/bedding angle and type and relative orientation of magnetic. Geological Society of America, Special Publication*.

Esquivel, E. V., Murr, L. E., Lopez, M. I., & Goodell, P. C. (2005). TEM observations of a 30 million year old mountain leather nanofiber mineral composite. *Materials Characterization*, *54*(4-5), 458–465. https://doi.org/10.1016/j.matchar.2005.01.014

Evans, M., Lewchuk, M., & Elmore, R. (2003). Strain partitioning of deformation mechanisms in limestones: Examining the relationship of strain and anisotropy of magnetic susceptibility (AMS). *Journal of Structural Geology*, *25*(9), 1525–1549. https://doi.org/10.1016/S0191-8141(02)00186-4

Eyal, Y. (1996). Stress field fluctuations along the Dead Sea rift since the middle Miocene. *Tectonics*, *15*, 157–170. https://doi.org/10.1029/95TC02619

Eyal, Y., & Reches, Z. (1983). Tectonic analysis of the Dead Sea rift region since the Late-Cretaceous based on mesostructures. *Tectonics*, *2*, 39–66.

Freund, R., Garfunkel, Z., Zak, I., Goldberg, M., Weissbrod, T., & Derin, B. (1970). The shear along the Dead Sea rift. *Philosophical Transactions of the Royal Society of London A*, *267*(1181), 107–130. https://doi.org/10.1098/rsta.1970.0027

Garfunkel, Z. (1981). Internal structure of the Dead Sea leaky transform (rift) in relation to plate kinematics. *Tectonophysics*, *80*(1-4), 81–108. https://doi.org/10.1016/0040-1951(81)90143-8

Garfunkel, Z. (2014). Lateral motion and deformation along the Dead Sea transform. *Dead Sea Transform Fault System: Reviews*. https://doi.org/10.1007/978-94-017-8872-4_5

Girdler, R. (1961). The measurement and computation of anisotropy of magnetic susceptibility of rocks. *Geophysical Journal of the Royal Astronomical Society*, *5*, 34–44.

Henry, B. (1983). Interprétation Quantitative de l'anisotropie de susceptibilité magnétique. *Tectonophysics*, *91*, 165–177.

Henry, B., & Daly, L. (1983). From qualitative to quantitative magnetic-anisotropy analysis—The prospect of finite strain calibration. *Tectonophysics*, *98*(3-4), 327–336. https://doi.org/10.1016/0040-1951(83)90300-1

Hirt, A. M., & Almqvist, B. S. G. (2011). Unraveling magnetic fabrics. *International Journal of Earth Sciences*, *101*(3), 613–624. https://doi.org/10.1007/s00531-011-0664-0

Hrouda, F. (2002). The use of the anisotropy of magnetic remanence in the resolution of the anisotropy of magnetic susceptibility into its ferromagnetic and paramagnetic components. *Tectonophysics*, *347*(4), 269–281. https://doi.org/10.1016/S0040-1951(02)00075-6

Hrouda, F. (2004). *Problems in interpreting AMS parameters in diamagnetic rocks. Geological Society of London, Special Publication*, *238*, 49–59.

Hrouda, F., Henry, B., & Borradaile, G. (2000). Limitations of tensor subtraction in isolating diamagnetic fabrics by magnetic anisotropy. *Tectonophysics*, *322*(3-4), 303–310. https://doi.org/10.1016/s0040-1951(00)00093-7

Hunt, C. P., Moskowitz, B. M., & Banerjee, S. K. (1995). Magnetic properties of rocks and minerals. In T. J. Ahrens (Ed.), *Rock physics phase relations a handbook physical constants* (Vol. 3, pp. 189–204). https://doi.org/10.1029/RF003

Issachar, R., Levi, T., Lyakhovsky, V., Marco, S., & Weinberger, R. (2016). Improving the method of low-temperature anisotropy of magnetic susceptibility (LT-AMS) measurements in air. *Geochemistry, Geophysics, Geosystems*, *17*, 2940–2950. https://doi.org/10.1002/2016GC006339

Issachar, R., Levi, T., Marco, S., & Weinberger, R. (2015). Anisotropy of magnetic susceptibility in diamagnetic limestones reveals deflection of the strain field near the Dead Sea Fault, northern Israel. *Tectonophysics*, *656*, 175–189. https://doi.org/10.1016/j.tecto.2015.06.021

Jackson, M. (1991). Anisotropy of magnetic remanence: a brief review of mineralogical sources, physical origins, and geological applications, and comparison with susceptibility anisotropy. *Pure and Applied Geophysics*, *136*(1), 1–28. https://doi.org/10.1007/bf00878885

Jelinek, V. (1981). Characterization of the magnetic fabric of rocks. *Tectonophysics*, *79*, T63–T67.

Levi, T., & Weinberger, R. (2011). Magnetic fabrics of diamagnetic rocks and the strain field associated with the Dead Sea Fault, northern Israel. *Journal of Structural Geology*, *33*(4), 566–578. https://doi.org/10.1016/j.jsg.2011.02.001

Levi, T., Weinberger, R., & Marco, S. (2014). Magnetic fabrics induced by dynamic faulting reveal damage zone sizes in soft rocks, Dead Sea basin. *Geophysical Journal International*, *199*(2), 1214–1229. https://doi.org/10.1093/gji/ggu300

Martin-Hernandez, F., & Ferre, E. C. (2007). Separation of paramagnetic and ferrimagnetic anisotropies: A review. *Journal of Geophysical Research*, *112*, B03105. https://doi.org/10.1029/2006JB004340

Nathan, Y., & Flexer, A. (1977). Clinoptilolite, paragenesis and stratigraphy. *Sedimentology*, *24*(6), 845–855. https://doi.org/10.1111/j.1365-3091.1977.tb01919.x

Nuriel, P., Weinberger, R., Kylander-Clark, A. R. C., Hacker, B. R., & Craddock, J. P. (2017). The onset of the Dead Sea transform based on calcite age-strain analyses. *Geology*, *45*(7), 587–590. https://doi.org/10.1130/G38903.1

Nye, J. F. (1957). In O. S. Publications (Ed.), *Physical properties of crystals: Their representation by tensors and matrices*. Oxford: Clarendon Press.
Oertel, G. (1983). The relationship of strain and preferred orientation of phyllosilicate grains in rocks—A review. *Tectonophysics*, *100*(1-3), 413–447. https://doi.org/10.1016/0040-1951(83)90197-X
Oliva-Urcia, B., Casas, A. M., Moussaid, B., Villalaín, J. J., El Ouardi, H., Soto, R., et al. (2016). Tectonic fabrics vs. mineralogical artifacts in AMS analysis: A case study of the Western Morocco extensional Triassic basins. *Journal of Geodynamics*, *94-95*, 13–33. https://doi.org/10.1016/j.jog.2016.01.004
Owens, W. H., & Rutter, E. H. (1978). The development of magnetic susceptibility anisotropy through crystallographic preferred orientation in a calcite rock. *Physics of the Earth and Planetary Interiors*, *16*(3), 215–222. https://doi.org/10.1016/0031-9201(78)90014-6
Palchik, V., & Hatzor, Y. (2002). Crack damage stress as a composite function of porosity and elastic matrix stiffness in dolomites and limestones. *Engineering Geology*, *63*, 233–245.
Parés, J. (2015). Sixty years of anisotropy of magnetic susceptibility in deformed sedimentary rocks. *Frontiers in Earth Science*, *3*, 4.
Parés, J. M., & van der Pluijm, B. A. (2002). Phyllosilicate fabric characterization by low-temperature anisotropy of magnetic susceptibility (LT-AMS). *Geophysical Research Letters*, *29*(24), 2215. https://doi.org/10.1029/2002GL015459
Parés, J. M., van der Pluijm, B. A., & Dinares-Turell, J. (1999). Evolution of magnetic fabrics during incipient deformation of mudrocks (Pyrenees, northern Spain). *Tectonophysics*, *307*(1-2), 1–14. https://doi.org/10.1016/S0040-1951(99)00115-8
Quennell, A. M. (1959). Tectonics of the Dead Sea rift. In *Congreso Geologico Internacional, 20th sesion, Asociacion de Servicios Geologicos Africanos* (pp. 385–405). Mexico City.
Rochette, P., Jackson, M., & Aubourg, C. (1992). Rock magnetism and the interpretation of anisotropy of magnetic susceptibility. *Reviews of Geophysics*, *30*, 209–226. https://doi.org/10.1029/92RG00733
Saruwatari, K., Ozaki, N., & Nagasawa, H. (2006). Letter: Crystallographic alignments in a coccolith (Pleurochrysis carterae) revealed by electron back-scattered diffraction (EBSD). *American Mineralogist*, *91*, 1937–1940.
Schmidt, V., Gunther, D., & Hirt, A. M. (2006). Magnetic anisotropy of calcite at room-temperature. *Tectonophysics*, *418*(1-2), 63–73. https://doi.org/10.1016/j.tecto.2005.12.019
Schmidt, V., Hirt, A. M., Leiss, B., Burlini, L., & Walter, J. M. (2009). Quantitative correlation of texture and magnetic anisotropy of compacted calcite-muscovite aggregates. *Journal of Structural Geology*, *31*(10), 1062–1073. https://doi.org/10.1016/j.jsg.2008.11.012
Schmidt, V., Hirt, A. M., Rosselli, P., & Martin-Hernandez, F. (2007). Separation of diamagnetic and paramagnetic anisotropy by high-field, low-temperature torque measurements. *Geophysical Journal International*, *168*(1), 40–47. https://doi.org/10.1111/j.1365-246X.2006.03202.x
Sneh, A., Bartov, Y., Weissbrod, T., & Rosensaft, M. (1998). Geological Map of Israel (scale 1: 200,000). Jerusalem: Geological Survey of Israel.
Sneh, A., & Weinberger, R. (2014). *Major Structures of Israel and Environs* (scale 1: 500,000).
Soto, R., Casas-Sainz, A. M., Villalain, J. J., & Oliva-Urcia, B. (2007). Mesozoic extension in the Basque-Cantabrian basin (N Spain): Contributions from AMS and brittle mesostructures. *Tectonophysics*, *445*(3-4), 373–394. https://doi.org/10.1016/j.tecto.2007.09.007
Till, J. L., Jackson, M. J., & Moskowitz, B. M. (2010). Remanence stability and magnetic fabric development in synthetic shear zones deformed at 500°C. *Geochemistry, Geophysics, Geosystems*, *11*, Q12Z21. https://doi.org/10.1029/2010GC003320
Vollmer, F. W. (2016). Orient 3: Spherical projection and orientation data analysis program.
Weinberger, R. (2014). Pleistocene strain partitioning during transpression along the Dead Sea Transform, Metulla Saddle, Northern Israel. *Dead Sea Transform Fault System: Reviews*. https://doi.org/10.1007/978-94-017-8872-4_6
Weinberger, R., Gross, M. R., & Sneh, A. (2009). Evolving deformation along a transform plate boundary: Example from the Dead Sea Fault in northern Israel. *Tectonics*, *28*, TC5005. https://doi.org/10.1029/2008TC002316
Young, J., Didymus, J., Bown, P., Prins, B., & Manns, S. (1992). Crystal assembly and phylogenetic evolution in heterococcoliths. *Nature*, *356*(6369), 516–518. https://doi.org/10.1038/356516a0